Measured Spatially Variant System Response for PET Image Reconstruction

Adam M. Alessio, *Member, IEEE,* , Paul E. Kinahan, *Senior Member, IEEE,*, Robert L. Harrison, *Member, IEEE,* and Thomas K. Lewellen, *Senior Member, IEEE*

***Abstract*— Quantitative accuracy in PET imaging is essential for longitudinal studies and monitoring tumor response to treatment. The goal of this work is to improve the quantitative accuracy of whole-body PET imaging through the use of an accurate, measured system model. Past empirically measured system response functions used line sources positioned at various locations in the imaging field of view. Here, we present a practical method for measuring the detector blurring component of a whole-body PET system with a non-collimated point source. We employ Monte Carlo simulations to show that a non-collimated point source is acceptable for modeling the radial blurring present in a PET tomograph. And, we justify the use of a Na22 point source for collecting these measurements. We measure the system response, simplify it to a two-dimensional function, and incorporate a parameterized version of this response into a modified OSEM algorithm. Reconstructions of measured data from an image quality and line source phantom reveal improved quantitative accuracy and resolution with the modified system model.**

***Index Terms*— PET, quantitation, statistical reconstruction, system modeling, PSF**

I. Introduction

The goal of this work is to improve the quantitative accuracy of whole-body PET imaging through the use of a more accurate system model. We present a practical method for measuring the detector blurring component of the system response with a non-collimated point source. We employ Monte Carlo simulations to show that a non-collimated point source is appropriate for modeling the radial blurring present in a PET tomograph. And, we justify the use of a Na22 point source for collecting system response measurements. We measure the system response, simplify it to a two-dimensional function, and incorporate a parameterized version of this response into a modified OSEM algorithm. Reconstructions of measured data from an image quality phantom reveal improved resolution with the modified system model.

Previous efforts have modeled the system response through analytical derivations, Monte Carlo simulations, and empirical measurements leading to improved resolution with high-resolution, small animal imaging systems. Past empirically measured system response functions used line sources positioned at multiple radial locations in the imaging field of view [1], [2]. Our previous work used Monte Carlo simulations of the system response and evaluated the potential improvements with a simulated system model [3]. Positive simulation results from our previous work motivated the empirical efforts in this current research. Here, we propose collecting measurements from a point source in a whole body scanner and perform an initial evaluation of the improvements with 2-D image reconstruction. These efforts are extendable for use with fully 3-D imaging.

The system model for a PET tomograph can be factorized into multiple components such as the geometric projection matrix (basis for all conventional models), attenuation correction factors, detector sensitivity factors, and detector blurring [4]. While the complete detector blurring component of a fully 3-D imaging system is a seven dimensional function, this work models the detector blurring as a 2-D system response function, $\mathbf{S}(s; s_v)$, that blurs in radial position, s, and is variant in radial position s_v. This term includes the effects of inter-crystal scatter, penetration, and, since it is a measured response, photon pair non-collinearity and positron range. Since this term includes more than just detector effects, we use the more general term "system response function" to describe a model with all of these effects. We assume rotational invariance of the detector geometry and invariance amongst axial planes; thus, the same response function be applied at all azimuthal angles and axial planes.

II. Collimated vs. Non-collimated

We propose using measured, empirical response data from a whole-body PET tomograph to better characterize the detector blurring component of the system response. An ideal experiment would employ a point source collimated to emit photons along a single line of response (LOR), revealing the blurring extent in each LOR. In reality, this experiment is not feasible because of: a) the number of LORs, b) the challenge of accurately positioning the point source and the collimation given the multiple degrees of freedom, and c) an appropriately collimated source results in significantly less photons requiring long scan times for each LOR.

The use of a non-collimated point source avoids these challenges; but, for 2-D imaging, data from a non-collimated point source does not contain information about blurring among azimuthal angles considering that all angles are collected during acquisition. In order to justify the use of the non-collimated

Manuscript received November 9, 2005. This work was supported by NIH grant CA74135 and CA42593.

Authors are with the Dept. of Radiology, University of Washington, Seattle, WA 98195 USA. (telephone: (206)598-4521, email: aalessio@u.washington.edu)

measured point source, we performed Monte Carlo simulations using the GATE package [5] to show that collimated and non-collimated point sources result in similar $\mathbf{S}(s;s_v)$ response functions. We simulated a dual photon emitting source in a highly accurate scanner model of the GE Advance [6], [7]. These measurements include the effects of scanner geometry, block effects, inter-crystal scatter, and penetration and were corrected to have equally spaced radial bins as performed on the Advance system.

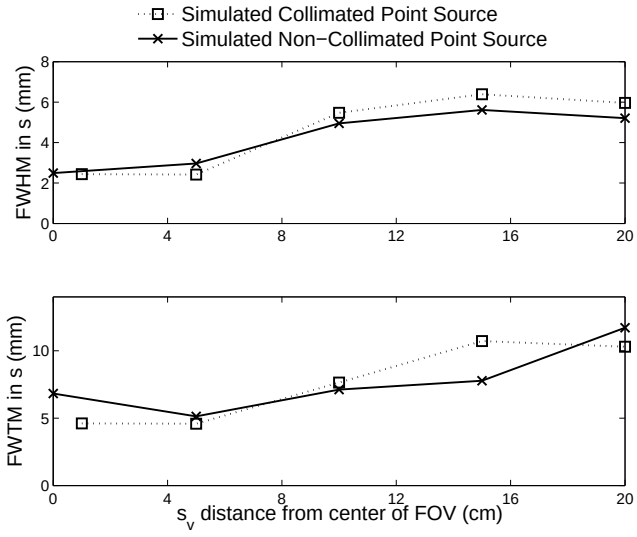

Fig. 1. FWHM and FWTM of $\mathbf{S}(s;s_v)$ formed from non-collimated and collimated point source at different locations.

Figure 1 plots the full width at half maximum (FWHM) and FWTM in s of the resulting $\mathbf{S}(s;s_v)$ from the point source positioned at different radial positions (varying s_v). These plots show results from 10 different simulations (collimated and non-collimated point source at 5 unique radial positions). The close agreement in these plots shows that a non-collimated point source is adequate for measuring the system response function $\mathbf{S}(s;s_v)$. The validity of this conclusion is further confirmed in figure 2 where the shape of the simulated non-collimated and collimated responses are shown to be very similar and match the measured response.

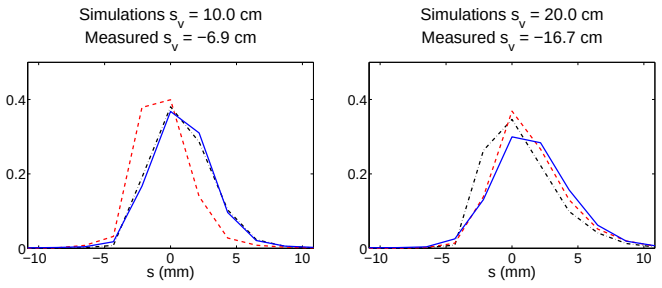

Fig. 2. Comparison of $\mathbf{S}(s;s_v)$ from simulated collimated (dash dot), simulated non-collimated (dash), and measured non-collimated (solid) point sources.

III. Positron Range of Point Source

A point source of one of the typical PET radioisotopes is difficult to fashion in a reproducible manner and the relatively short half life complicates a longer experiment needed to characterize the system. Consequently, we used a solid Na22 source (half life=2.6 years) of size $\sim$0.25mm diameter embedded in Lucite.

One concern with using the Na22 source is its potentially different positron range than common PET isotopes. We used a modification of the SimSET simulation package to model the positron range of Na22 and F18 based on the Palmer and Brownell parameterized model [8]. Rather than following the positron trajectory until is reaches thermal energy [9], this model assumes that the equilibrium particle density resulting from a point source of monoenergetic positrons can be represented by a three-dimensional Gaussian distribution centered at the origin. We modified SimSET in the past to include positron range for several common nuclear medicine isotopes [10] and this works added Na22 to the list of available isotopes.

We simulated the positron end points of F18 in water (typical scanned object) and Na22 in Lucite (our method for measuring response). Figure 3 shows the calculated positron annihilation coordinates in various representations (projection of 3D positron end-point cloud projected onto a plane, a single axis, and a histogram of positron distances). These plots reveal that the positron ranges for F18 and our proposed source are very similar and justify the use of Na22 for system response function measurements.

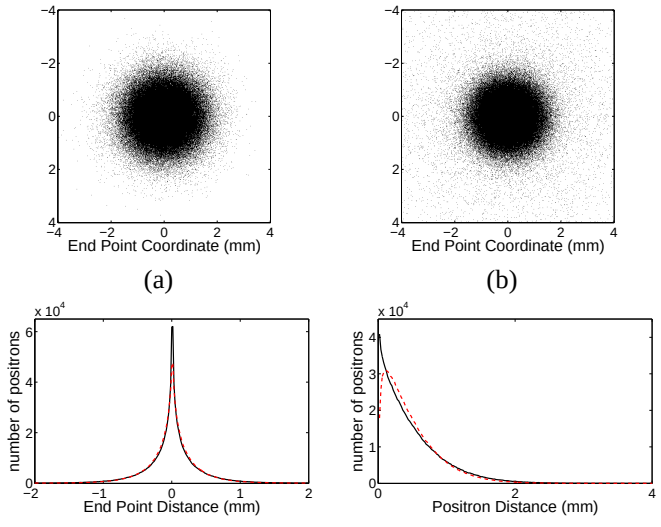

Fig. 3. Comparison of positron range of F18 in water (a) and Na22 in Lucite (b). Binary images (a) and (b) show positron annihilation coordinates projected on a single axis. Plot (c) shows the projection of (a) and (b) onto a single axis with F18 (solid) and Na (dashed). The histogram (d) reveals of positron distance of F18 (solid) and Na (dashed).

IV. Measuring the SRF

We positioned the Na22 point source at varying radial positions in a GE Advance tomograph and collected 2-D

measurements. For each measurement, the radial profile through the angle of the sinogram resulting in the most extreme radial locations formed the known system response function at set locations. Figure 4 plots the measured $\mathbf{S}(s; s_v)$ at 4 radial locations, $s_v = [-1.5, -6.9, -13.2,\text{and} -17.1]$cm. These plots show that the response is more broad and more asymmetric at locations away from the center of the field of view (FOV).

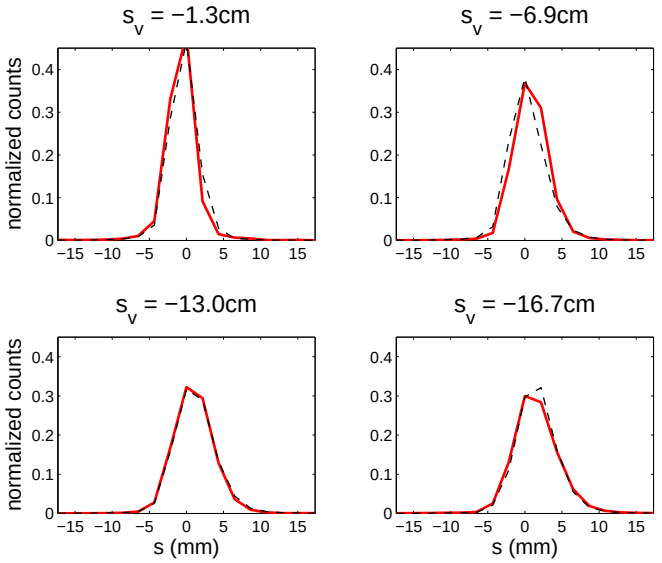

Fig. 4. Measured system response in s to Na22 point source positioned at 4 locations, s_v shown in solid line. The parameterized version shown in dotted line.

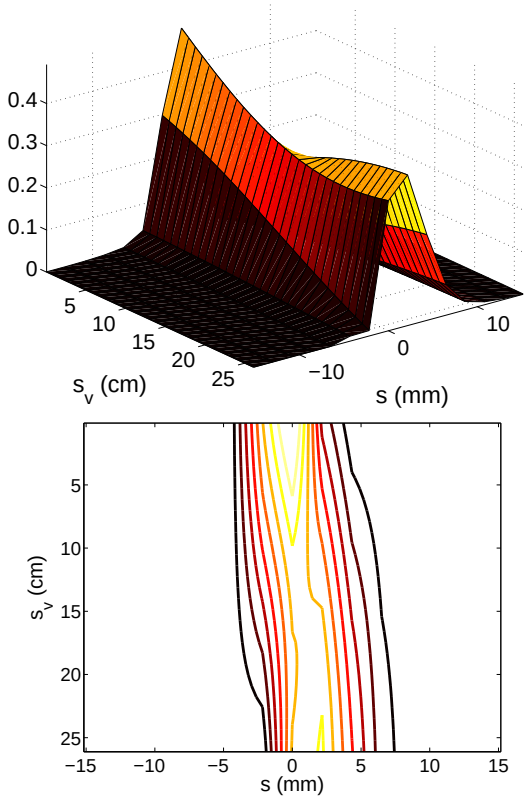

Fig. 5. Mesh and contour plot of complete $\mathbf{S}(s; s_v)$ for 0 to 25 cm from the center of FOV formed from parameterizing the measured $\mathbf{S}$ values and completing the function for all radial positions s_v.

In order to find the system response functions at all radial locations, these known functions were parameterized with their discrete cosine transform coefficients. We found a linear fit amongst all the coefficients to determine the system response at all radial locations. We found that only 4 different measurements (at different radial locations) were adequate to provide a thorough characterization of this function. Figure 5 presents the complete $\mathbf{S}(s; s_v)$ for radial locations in one half of the field of view. Assuming symmetry, this function is flipped in s for the other half of the field of view. We originally proposed this approach for 3D system responses derived from simulations [3].

V. Applying SRF in Reconstruction

We used the measured system response function to modify the conventional system matrix in the OSEM algorithm [11] and denote the new method as OSEM+$\mathbf{S}$. In 2D imaging, the system matrix can be described as a 6 dimensional function, $\mathbf{P}()$, which relates the image/volume space (with coordinates x_v, y_v, z_v) to the projection space with radial bin, s, azimuthal angle bin, ϕ, and axial location z. With this formulation, the 2D measured response modifies the system matrix through a convolution in s as

$$\hat{\mathbf{P}}(s_v, \phi, z; x_v, y_v, z_v) = \sum_{s'} \mathbf{S}(s_v - s'; s_v)\mathbf{P}(s', \phi, z; x_v, y_v, z_v). \quad (1)$$

The applied $\mathbf{S}$ was a kernel with 11 bins in s that varied at each s_v. This blurring term could be included in a factorized system model and applied during each call to the system matrix [12]. In contrast, we precompute the system matrix and perform this convolution for each s_v only once storing the modified system matrix in memory in a sparse data format.

VI. Evaluation

A. NEMA IEC Phantom

We tested the measured system response and modified OSEM algorithm with measured data from the NEMA IEC body phantom. The phantom consists of a semi-anthropomorphic chamber and 6 internal spheres (1.0 to 3.7 cm diameters) filled with F18 with a tumor to background ratio of 8:1. We did not use the optional cold-spot cylindrical insert. We collected 2D measurements of this phantom on the GE Advance and fully corrected the raw data (arc, measured attenuation, normalization, and well counter corrections) prior to reconstruction.

Figure 6 presents reconstructions of the NEMA IEC body phantom with conventional FBP, OSEM and the modified OSEM. The FBP reconstructions were formed with a 100% cutoff Hanning window and the OSEM methods were reconstructed with 13 iterations, 12 subsets, and post-smoothed with a 2.5mm FWHM 3D Gaussian filter. These reconstructions have

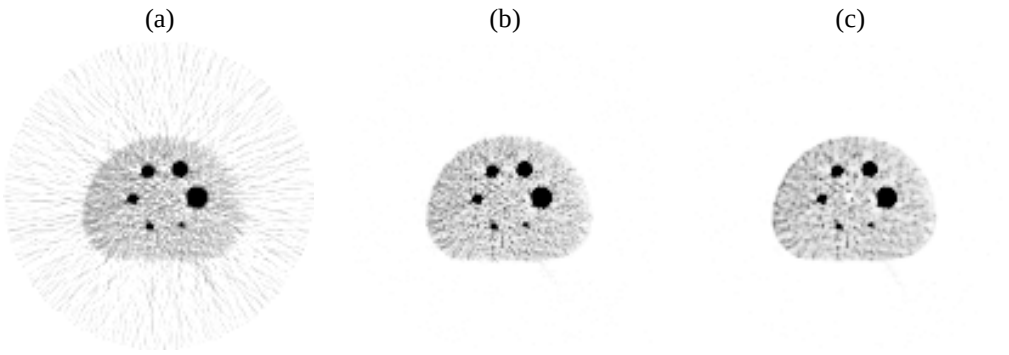

Fig. 6. Transaxial slice through reconstructions of measured data using FBP (a), OSEM (b) and OSEM+**S**(c). All reconstructions have matched standard deviations in the background activity regions.

matched standard deviations in the background activity regions with these noise regularization settings.

Figure 7 highlights the quantitative improvements with the use of $\mathbf{S}(s; s_v)$. The percent error in the average sphere values is calculated from averaging all of the voxels fully inscribed in the spheres and dividing by the true value of the sphere. The true value is formed by multiplying the average background value by 8. Figure 7a presents plots when less noise is acceptable (equivalent to 10mm Gaussian post-smoothing) and figure 7b is formed from the reconstructions shown in figure 6. Essentially, when the reconstructions are heavily regularized (smoothed) there is less of a quantitative benefit with the modified OSEM. The average percent error over all 6 spheres for fig 7a with FBP is 0.56, conventional OSEM is 0.46, and with OSEM+**S** is 0.44. When the reconstructions are less regularized (fig.7b) the average error for FBP is 0.29, OSEM is 0.26, and OSEM+**S** is 0.21. The relatively minor improvements with OSEM+**S** may be due to the fact that all spheres are at the same radial distance close to the center, diminishing the benefit of the improved resolution response at radial locations further from the center.

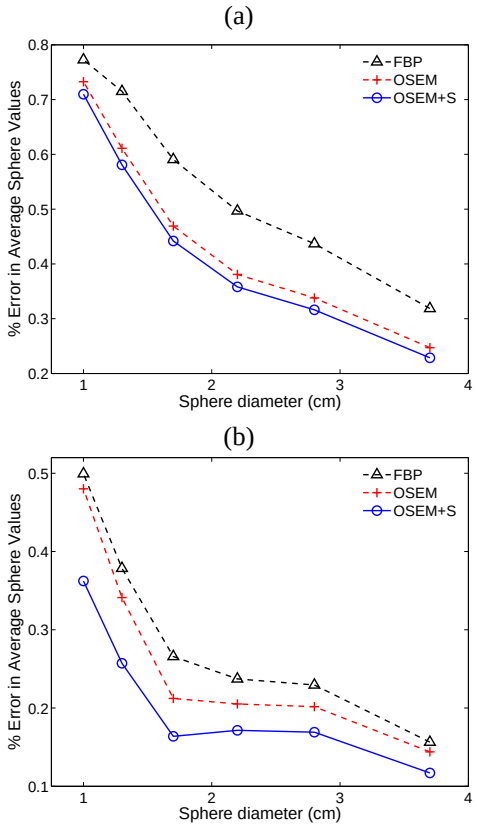

Fig. 7. Quantitative accuracy of each feature in the NEMA IEC Body phantom plotting the error in the average of voxels inside the spheres versus sphere size. Plot (a) is formed from images regularized with 10mm post-smoothing and (b) from images regularized with 2.5mm post-smoothing.

B. Line Source Phantom

We constructed a custom line source phantom consisting of an elliptical chamber (30cm long axis, 22cm short axis, and 18cm deep). An acrylic frame was suspended in the elliptical chamber to support multiple lengths of tubing (12cm long, 0.8mm internal diameter). The tubing essentially formed 8 line sources 3.5cm apart (see figure 8). The line sources were filled with F18 with a line to background chamber ratio of $\sim$150:1. We collected 2D measurements of this phantom positioned off-center on the GE Advance and fully corrected the raw data prior to reconstruction.

Reconstructions of the line source phantom were regularized with 10mm smoothing to have matched standard deviations in the background regions. The noise in a single transaxial slice made it difficult to assess the resolution improvements with the small sources in background activity. Figure 9 shows the sum of 10 transaxial slices through the full reconstruction. Figure 10 presents a profile through these summed images and shows that the proposed OSEM+**S** method results in higher line source

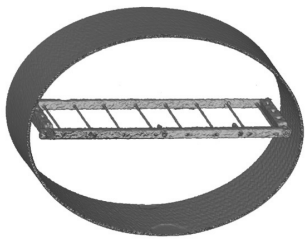

Fig. 8. Volume rendered image of CT scan of line source phantom showing the 8 line sources supported by a plastic frame.

values with the same background levels. Figure 11 presents a systematic analysis of resolution plotting the average FWHM of profiles drawn through two longest axes of each point. This plot shows that conventional OSEM results in resolution that degrades towards the edge of the FOV. On the other hand, the proposed method removes most of this variance in resolution response.

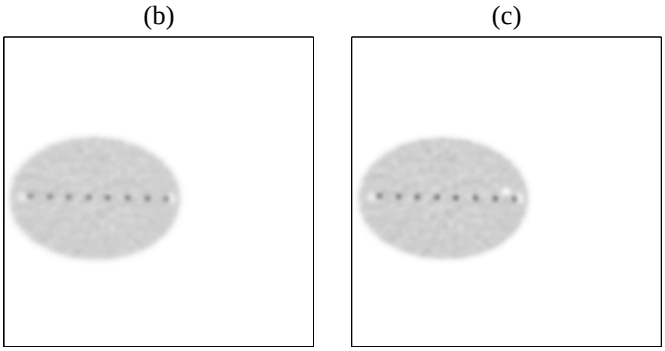

Fig. 9. Sum of 10 transaxial slices through reconstructions of measured line source data using OSEM (a) and the proposed OSEM+**S**. All reconstructions have matched standard deviations in the background activity regions.

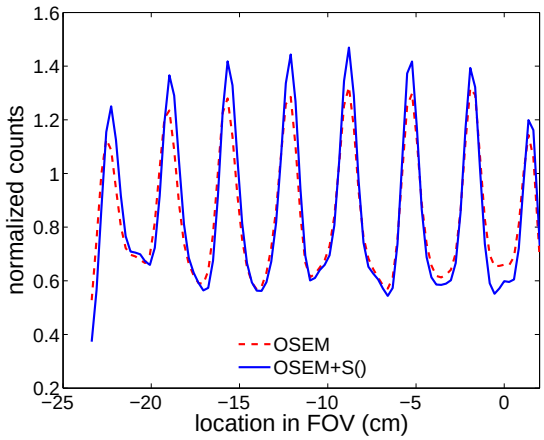

Fig. 10. Horizontal profile through summed transaxial images shown in figure 9 plotted along radial location in FOV.

VII. Discussion and Conclusion

Our previous work used simulations to show the benefits of a simulated system matrix both in terms of resolution and variance across multiple realizations [3]. This current work expanded upon the previous simulation studies and empirically measured the system response function and applied this function to empirical, not simulated, data sets. In the measured NEMA IEC body reconstructions, at matched background standard deviations, the proposed OSEM+**S** yielded quantitative improvements over conventional OSEM of ∼23%. This improvement is in keeping the expected improvement of approximately 15% derived from our previous rigorous simulation studies at this noise level. Moreover, the line source phantom showed that the proposed reconstruction method removes the

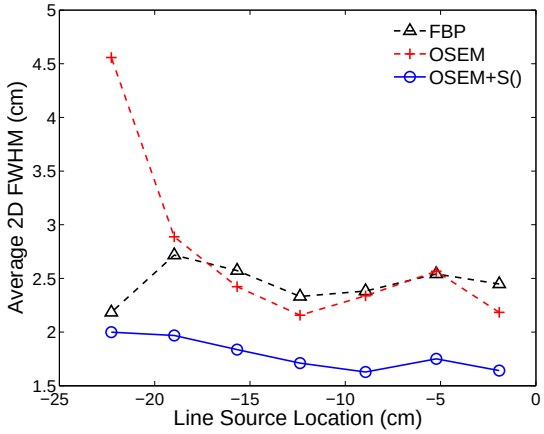

Fig. 11. FWHM versus line source location computed from images in figure 9

variant resolution response and at 10mm smoothing improved the FWHM resolution by ∼20% at the center of the FOV and ∼40% at the edge of the FOV. These positive results support the efficacy of the proposed method for measuring the system response with a non-collimated Na22 point source and using this response in a modified OSEM algorithm.

References

[1] T. Frese, N. Rouze, C. Bouman, K. Sauer, and G. Hutchins, "Quantitative comparison of FBP, EM, and Bayesian reconstruction algorithms for the IndyPET scanner," *IEEE Trans Med Imaging*, vol. 22, no. 2, pp. 258–76, 2003.

[2] K. Lee, P. Kinahan, J. Fessler, R. Miyaoka, M. Janes, and T. Lewellen, "Pragmatic fully 3D image reconstruction for the MiCES mouse imaging PET scanner," *Physics in Medicine and Biology*, vol. 49, no. 19, p. 4563, 2004.

[3] A. Alessio, P. Kinahan, and T. Lewellen, "Modeling and incorporation of system response functions in 3D whole body PET," *submitted to IEEE Trans Med Imaging*, 2005.

[4] J. Qi, R. Leahy, S. Cherry, A. Chatziioannou, and T. Farquhar, "High-resolution 3D Bayesian image reconstruction using the microPET small-animal scanner," *Physics in Medicine and Biology*, vol. 43, no. 4, p. 1001, 1998.

[5] S. Jan, G. Santin, D. Strul, and et al., "GATE: a simulation toolkit for PET and SPECT," *Physics in Medicine and Biology*, no. 19, pp. 4543–4561, 2004.

[6] C. Schmidtlein, A. Kirov, S. Nehmeh, and et al., "Validation of GATE Monte Carlo simulations of the GE Advance/Discovery LS PET scanners," in *AAPM*, Seattle, 2005.

[7] ——, "Validation of GATE Monte Carlo simulations of the GE Advance/Discovery LS PET scanners," *submitted to Med Phys*, 2005.

[8] M. Palmer and G. Brownell, "Annihilation density distribution calculations for medically important positron emitters," *IEEE Trans Med Imaging*, vol. 11, no. 3, pp. 373–378, 1992.

[9] C. Levin and E. Hoffman, "Calculation of positron range and its effect on the fundamental limit of positron emission tomography system spatial resolution," *Physics in Medicine and Biology*, no. 3, pp. 781–799, 1999.

[10] R. Harrison, M. Kaplan, S. Vannoy, and T. Lewellen, "Positron range and coincidence non-collinearity in SimSET," in *IEEE Nuclear Science Symposium*, vol. 3, 1999, pp. 1265–1268.

[11] H. Hudson and R. Larkin, "Accelerated image reconstruction using ordered subsets of projection data," *IEEE Trans Med Imaging*, vol. 13, no. 4, pp. 601–609, 1994.

[12] E. Mumcuoglu, R. Leahy, S. Cherry, and E. Hoffman, "Accurate geometric and physical response modelling for statistical image reconstruction in high resolution PET," in *Proc. of IEEE Nucl. Sci. Symp. and Med. Imaging Conf.*, vol. 3, 1996, pp. 1569–1573.